Beneficial effects of 3D structured electrodes for the fast-charging of lithium-ion batteries

Vittorio De Lauri,[†,‡,¶] Lukas Krumbein,[†,‡] Simon Hein,[†,‡] Benedikt Prifling,[§] Volker Schmidt,[§] Timo Danner,[*,†,‡] and Arnulf Latz[†,‡,‖]

†*German Aerospace Center (DLR), Institute of Engineering Thermodynamics,Pfaffenwaldring 38-40,70569 Stuttgart, Germany*

‡*Helmholtz Institute for Electrochemical Energy Storage (HIU), Helmholtzstraße 11, 89081 Ulm, Germany*

¶*University of Modena and Reggio Emilia, Via Universita 4, 41121 Modena, Italy*

§*Ulm University (UUlm), Institute of Stochastics, Helmholtzstraße 18, 89081 Ulm, Germany*

‖*Ulm University (UUlm), Institute of Electrochemistry, Albert-Einstein-Allee 47, 89081 Ulm, Germany*

E-mail: timo.danner@dlr.de

Abstract

Lithium-ion batteries are the dominating electrochemical energy storage technology for battery electric vehicles. However, additional optimization is needed to meet the requirements of the automotive industry regarding energy density, cost, safety and fast charging performance. In conventional electrode designs there is a trade-off between energy density and rate capability. Recently, 3D structuring techniques, such as laser perforation, were proposed to optimize both properties at the same time and remarkable improvements in fast-charging performance have been demonstrated. In this

work we investigate the effect of structuring techniques on the thermal properties and electrochemical performance of the battery using microstructure resolved simulations. Particular attention will be paid to the heat evolution and lithium plating during fast-charging of the batteries. According to our results, 3D structuring is able to reduce the overall cell resistance by improving the electrolyte transport. This has a positive impact on the fast charging capability of the cell and, moreover, reduces the danger of lithium plating.

Keywords

Lithium-ion battery, Microstructure resolved simulation, Fast charging, Laser perforation, Lithium plating

1 Introduction

Global warming, increase of the greenhouse gas emissions, and scarcity of conventional energy sources are some of the most fundamental challenges for present and future generations.[1] Furthermore, the increasingly poor air quality registered in the big cities around the world has led several countries, such as Norway, Sweden, the Netherlands, India and China, to set ambitious targets to increase the share of emission-free cars. Moreover, sale of vehicles with conventional combustion engines is planned to be very much restricted or forbidden in the next 10-20 years.[2] As a consequence, the increasing share of electric vehicles (EVs) in the transport sector has received considerable attention, leading to an exponential growth of the total EV production in the last few years.[3]

The high energy and power density combined with a long life-time has made lithium-ion batteries the dominating electrochemical energy storage technology in the past decade. Moreover, the lithium-ion battery (LIB) has been the most successful battery for EVs so far and also seems to be one of the most promising technologies for the near future. However, the

number of EVs is still not comparable to the huge number of sold cars with conventional combustion technology. In fact, many properties of LIBs need to be improved. Main issues are limitations of energy density, cost, safety and fast charging performance. Especially, improvements in the latter are considered to be crucial to improve the acceptance of EVs in the market.[4–8] The fast-charging of LIBs to a state-of-charge close to 80% in less than 15 minutes is generally regarded as a minimum target in the automotive sector.

The goal of performance improvement and cost reduction of LIBs has led to different and novel battery concepts. For instance, a higher energy density can be achieved by increasing the areal capacity through larger electrode thickness or higher electrode density. With this approach the share of passive materials (current collectors, separators, etc.) can be decreased, thus improving the energy density and reducing material cost.[9] Furthermore, fewer cutting and stacking steps for the electrode sheets are needed, which potentially enables a reduction of costs in the battery production process.[10]

However, increasing the active material loading can cause transport limitations which also reduce the practical capacity and fast-charging capability of the cell.[11–14] In fact, thicker electrodes lead to longer transport pathways for lithium ions and, thus, to a drastic increase of the internal resistance.[15] Moreover, concentration gradients across the two electrodes lead to a low utilization of the active material.[8] This highlights the dilemma in electrode development where all aspects need to be addressed at once.

One route towards batteries with higher energy density and at the same time sufficient fast-charging capabilities is a 3D structuring of the electrodes. Previous studies[8,16–22] have highlighted that electrode structuring is indeed an efficient strategy to reduce mass transport limitations. Chen *et al.*[8] and more recently Kriegler *et al.*,[16] demonstrated that batteries with electrode microstructures modified by laser treatment allow charging rates as high as 6C which is even beyond the current targets of the battery program of the US Department of Energy.[23] Furthermore, similar studies using laser perforation and mechanical structuring techniques are presented in the literature[24,25] and some authors even investigate the appli-

cation of such techniques in industrial LIB manufacturing processes.[10,26] The experimental work on laser structuring of electrodes is also supported by simulation studies using continuum models to reproduce the experimental setup[8,17,24] and identify optimal parameters and configurations.[27,28] These studies demonstrate that perforation creates a hierarchical pore network with macroscopic transport pathways between anode and cathode which reduces concentration gradients and improves the performance of the cell. Mai et al.[28] use a 2D model in order to optimize different structuring parameters and demonstrate that structuring of anode and cathode provides the best performance assuming ideally aligned trenches. However, the 2D setup is not suitable for hole geometries which generally reduce the removal of active material. Moreover, in all previous simulation work[8,17,24,27,28] homogenized models are used which do not resolve the actual electrode microstructure. Therefore, these models neglect important microstructural features like the shape and size distribution of active material particles or anisotropic transport in the electrolyte due to the electrode microstructure. All of these aspects potentially have a strong effect on the occurrence of lithium plating during fast-charging. Finally, heat generation and removal is an important issue during fast-charging and has to our knowledge not been addressed in simulation studies of laser-structured electrodes.

In this paper we present microstructure resolved electrochemical-thermal simulations of battery cells consisting of NMC_{111} cathodes and graphite anodes. Virtual but realistic electrode microstructures are generated by stochastic 3D microstructure models, which are calibrated by tomographic image data obtained by synchrotron tomography. Spatially resolved electrochemical simulations therefore intrinsically take into account the structural aspects related to particle morphology or anisotropic transport. The electrochemical simulations are performed with the 'Battery and Electrochemistry Simulation Tool'[29] (BEST) which is based on several models previously developed by our group.[30–32] An overview of the simulation methodology is presented in Section 2. In particular, we investigate the effect of laser perforation on the electrochemical and thermal properties of electrodes and cells. Results of our simulations

are presented in Section 3. First, we set a focus on performance aspects, demonstrating superior fast-charging properties of perforated electrodes. Moreover, the simulations allow to assess the risk of lithium plating during high charging currents. We investigate the risk of lithium plating both for ideally isothermal conditions as well as in thermal simulations taking into account heat generation. Finally, we investigate the effect of processing related parameters, such as hole shape and relative hole position, on cell performance. Our study provides detailed insights of the transport processes in hierarchically structured electrodes and cells which sets the ground for future optimization of structuring concepts for high energy electrodes in lithium-ion batteries.

2 Simulation methodology

In this section we provide details on our simulation approach. First, the governing equations of our 3D model will be described (Section 2.1). Moreover, we give additional information on parameters (Section 2.2), electrode microstructures (Section 2.3), and simulation setup (Section 2.4).

2.1 Model description

In our simulations we use the Battery and Electrochemistry Simulation Tool BEST which is developed in collaboration between the DLR Institute of Engineering Thermodynamics and the Fraunhofer Institute for Industrial Mathematics (ITWM).[29] The models are based on the general principles of non-equilibrium thermodynamics and a detailed derivation can be found in our previous publications.[30–32] Table 1 summarizes the complete set of equations for the simulation of mass, charge and heat transport within NMC_{111}-graphite cells investigated in this work. In the remainder of this paragraph we provide a brief description of the model equations.

Eq. 1 describes the temporal evolution of lithium ion concentration in the electrolyte. The

corresponding fluxes of lithium ions are mainly given by three contributions. I) A diffusive flux due to Li-ion concentration gradients, II) migration due to the electric field or gradient in potential, respectively, and III) a flux due to temperature gradients in the electrolyte phase. Similarly, Eq. 4 tracks the lithium concentration in the active material phase due to concentration and temperature gradients.

Eq. 2 describes the charge conservation equation in the electrolyte phase. It can be derived in the same manner as Eq. 1 under the assumptions of charge neutrality and a fully dissociated binary salt. Eq. 5 is the charge conservation equation in the solid phase which basically reduces to Ohms law for the calculation of the solid potential distribution.

In the equations described above temperature gradients affect the transport in the different materials. Eq. 3 is the energy balance in the electrolyte which is used to calculate the temperature distribution. The temperature in the electrolyte can change due to thermal conduction and two different heat sources. Namely, Joule's heat and the heat of mixing. Similarly, Eq. 6 is used to calculate the temperature distribution in solid materials.

Eqs. 7-10 are the interface conditions and are required to couple the transport in electrolyte and active particles. Eq. 7 describes the intercalation and deintercalation reactions between active material and electrolyte as derived in Latz *et al.*[31] Eq. 8 is derived starting from the energy balance by integration over an infinitesimal small volume element. The terms on the right-hand side of Eq. 8 are given by an irreversible heat production due to Joule heating and the heat of mixing.

Note that in the original derivation of our model,[30,32] additional terms describing the Thomson and Soret effect are also included in the final energy balance. The effect of the different contributions is analyzed in Ref.[32] However, to the best of our knowledge Seebeck (β_e, β_s) and Soret-Dufour coefficients (k_T) of battery materials are not reported and are often neglected in the literature.[32,33] Therefore, we also do not consider these effects in the simulations presented in this paper.

Table 1: Governing equations for thermal simulations of NMC_{111}-graphite cells.

Electrolyte	
Material balance	$$\frac{\partial c_e}{\partial t} = \nabla \cdot (D_e \nabla c_e) - \nabla \cdot \left(\frac{t_+}{z_+ F} \vec{j} \right) \quad (1)$$
Charge balance	$$0 = \nabla \cdot (\varkappa \nabla \varphi_e) - \nabla \cdot \left(\varkappa \frac{1 - t_+}{z_+ F} \frac{\partial \mu}{\partial c} \nabla c_e \right) - \nabla \cdot \left(\frac{\varkappa}{z_+ F} \left(\frac{\partial \mu}{\partial T} \right) \nabla T \right) \quad (2)$$
Energy balance	$$c_{p,e} \rho \frac{\partial T_e}{\partial t} = \nabla \cdot (\lambda_e \nabla T) + \frac{\vec{j}^2}{\varkappa} + \left(\frac{\partial \mu}{\partial c} \right) \frac{\left(\vec{N_+} - \frac{t_+}{F z_+} \vec{j} \right)^2}{D_e} \quad (3)$$
Active material	
Material balance	$$\frac{\partial c_s}{\partial t} = \nabla \cdot (D_s \nabla c_s) \quad (4)$$
Charge balance	$$0 = \nabla \cdot (\sigma \nabla \Phi_s) \quad (5)$$
Energy balance	$$c_{p,s} \rho \frac{\partial T_s}{\partial t} = \nabla \cdot (\lambda_s \nabla T) + \frac{\vec{j}^2}{\varkappa} - z_+ F \frac{\partial U_0}{\partial c} \frac{\vec{N_+}^2}{D_s} \quad (6)$$
Interface conditions	
Butler-Volmer	$$i_{se} = i_{00}' \cdot c_{el}^{\alpha_a} \cdot c_s^{\alpha_a} \left(\exp \left[\frac{\alpha_a F}{RT} \eta_s \right] - \exp \left[\frac{-\alpha_c F}{RT} \eta_s \right] \right) \quad (7)$$
Energy balance	$$-\lambda_s \vec{n} \cdot \vec{\nabla} T_s + \lambda_e \vec{n} \cdot \vec{\nabla} T_e = -i_{se} \eta_s - T i_{se} \left\{ \frac{\partial \left(U_0 + \frac{\mu_e}{z_+ F} \right)}{\partial T} \right\} \quad (8)$$
Ionic flux	$$\vec{j_s} \cdot \vec{n} = i_{se} \text{ and } \vec{j_e} \cdot \vec{n} = i_{se} \quad (9)$$
Electric current	$$\vec{N}_{+,s} \cdot \vec{n} = \frac{i_{se}}{z_+ F} \text{ and } \vec{N}_{+,e} \cdot \vec{n} = \frac{i_{se}}{z_+ F} \quad (10)$$

2.2 Model parametrization

For the model described above, material, transport, and kinetic parameters need to be defined. With our simulations we aim at a qualitative understanding of the effect of perforation on performance and degradation. Therefore, we compile sets of parameters for the

materials of interest provided in the literature. A description of the different parameters as function of concentration and temperature is provided in the supporting information in Section S-2. Additionally, we report all parameters at room temperature (298 K) and for a fully discharged cell ($c_e = 1100 \cdot 10^{-6}\,mol/cm^3$, $c_{graphite} = 716.13 \cdot 10^{-6}\,mol/cm^3$ and $c_{NMC_{111}} = 27118.74 \cdot 10^{-6}\,mol/cm^3$) in Table 2.

Table 2: Transport, kinetic and thermodynamic parameters at room temperature and at the beginning of the charging simulations.

Parameter	Description	Electrolyte	NMC_{111}	Graphite	Ref.
D	Diffusion coefficient [$cm^2\,s^{-1}$]	2.3755e-6	7.6581e-11	3.4558e-10	[34–36]
$\varkappa$	Ionic conductivity [$mS\,cm^{-1}$]	7.8	-	-	[34]
σ	Electronic conductivity [$S\,cm^{-1}$]	-	100e-2	100e-2	-
t_+	Transference number [-]	0.1929	-	-	[34]
f	Activity coefficient [-]	1.505	-	-	[34]
U_0	Open circuit potential [V]	-	3.5	0.5	-
C^{dl}	Double layer capacitance [$F\,cm^{-2}$]	-	80.23e-4	0.92e-4	[35]
i'_{00}	BV prefactor [$A\ cm\,mol^{-1}$]	-	0.049	0.0254	[33,37]
c_p	Specific heat [$J\,kg^{-1}\,K^{-1}$]	1647.7	803.588	759	[38,39]
λ	Thermal conductivity [$W\,cm^{-1}\,K^{-1}$]	0.0017	0.0175	0.1091	[38,39]
ρ	Density [$kg\,cm^{-3}$]	1249e-6	4476e-6	2310e-6	[39]

Electrolyte Transport parameters for an electrolyte consisting of $LiPF_6$ in EC:DEC (1:1, by weight) were measured by Lundgren *et al.*[34] with salt concentrations between 0.5 and 1.5M and at temperatures between 10 and 40 °C. In our simulations we observe concentrations exceeding this range and, therefore, extrapolate the data to higher concentrations. The resulting set of parameters and corresponding correlations can be found in the supporting information in Section S-2.

Separator In our simulations we model a separator with a thickness of 25 µm and an effective conductivity of 18.4% of the bulk electrolyte conductivity which is representative for the family of Celgard separators.[40] Additionally, for the thermal model we also need the heat capacity ($1.75\,kJ\ kg^{-1}\ K^{-1}$)[38] and thermal conductivity ($0.002\,W\ cm^{-1}K^{-1}$) of typical

separator materials. Finally, the density was set to 989.6 kg m^{-3}, according to Werner *et al.*[39]

NMC_{111} Positive electrodes consist of NMC_{111} particles and a collection of relevant electrode properties is provided in Table 2. Among the different parameters the electronic conductivity σ and the double layer capacitance C_{dl} are constant in the simulations due to a lack of temperature dependent data in the literature. Moreover, we neglect the temperature dependence of the OCV which is generally minor and only observable at low SoC.[41,42] The OCV is parametrized based on our previous research.[14] The corresponding correlation is given in the supporting information.

Graphite The negative electrode consists of layered graphite particles and all relevant parameters related to the material are included in Table 2. Correlations describing the temperature dependence of the electronic conductivity σ and the OCV are not reported in the literature. Moreover, we assume a constant capacitance C_{dl}. The OCV of graphite is given in the supporting information.

2.3 Electrode microstructures

Electrode microstructures used in this paper are created by stochastic 3D microstructure models. In particular, the cathode has been generated by the stochastic modelling framework presented in Ref.[43], where the target volume fraction of active material equals 50%. The number-based radius distribution is given by a Gamma distribution with shape parameter 3.94 and rate parameter 2.17 µm^{-1}, leading to a volume-based d_{50}-diameter of 5.9 µm. After discretizing the non-spherical particles, which are modelled by Gaussian random fields on the sphere[44], a morphological closing is applied, where the structuring element is given by a ball with a radius of two voxel sizes. The anode is modelled by an excursion set of a Gaussian random field.[45,46] This modelling approach has been already used to simulate the anode morphology in Ref.[47], where the volume fraction of active material is now given by 60 %.

In both cases, the voxel size equals 0.876 µm. The microstructures consist of active material and a homogeneous carbon black and binder domain (CBD). The CBD has a significant effect on transport processes within the electrode.[48] We assume that the CBD is located closely to contact points of the active material particles which we identified as most probable configuration in our previous work.[48] The effective ionic conductivity in the CBD is assumed to be 10% of the bulk electrolyte conductivity.[47,49] We observe a percolating network of CBD for transport of electrons and therefore assume constant electronic conductivity in the solid phase given in Table 2.

The trend in lithium ion battery development is going towards higher areal loadings to improve energy density.[9] Therefore, we chose areal capacities of 4.25 and 3.5 mAh cm^{-2} for anode and cathode sheets, respectively. The density of our electrodes is $1.48 g \cdot cm^{-3}$ for the anode and $2.42 g \cdot cm^{-3}$ for the cathode, resulting in 88 µm and 100 µm electrode thickness, respectively.

Recall that the scope of this study is the investigation of the effect of laser perforation on cell performance, especially for fast charging scenarios. Therefore, we virtually perforate electrode sheets by removing active material and binder within an ideal cylinder with defined hole diameter. We choose a square grid with a hole distance of 200 µm and cylindrical holes with a diameter of 40 µm. The properties are in line with values reported in literature.[8,16] These parameters result in a capacity loss of ≈ 0.13 mAh cm^{-2} (3.1%).

In experiments typically conical holes are observed.[8,16] Therefore, we additionally investigate the effect of the hole geometry removing active material and binder in conically shaped holes with different angles. The volume of the holes is the same resulting in electrodes with the same nominal capacity.

2.4 Simulation setup

In this study we perform impedance spectroscopy simulations on symmetric cells as well as galvanostatic charge and discharge simulations on half- and full cells. In all cases we simulate

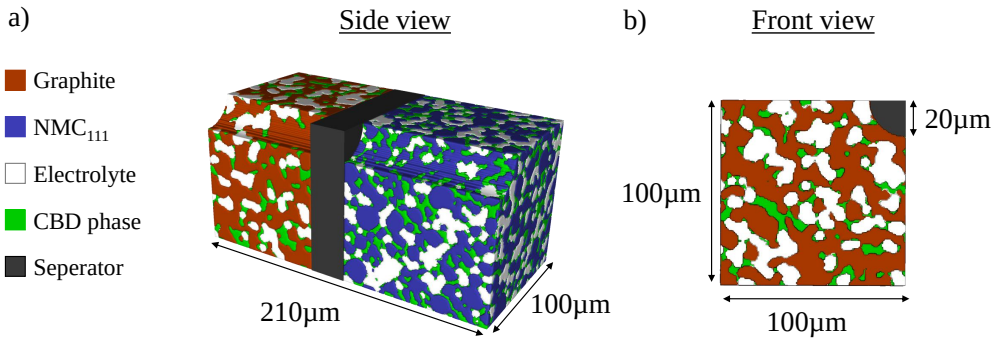

Figure 1: a) Simulation domain of a perforated full cell with graphite anode (red color) and NMC_{111} cathode (blue color). CBD is shown in both electrodes in green and the separator is shown in dark grey color. The electrolyte inside the perforation hole is transparent. b) View on the perforated graphite electrode in through direction (x).

both perforated and unperforated electrodes in order to evaluate the effect of the peroration on cell properties. Depending on the setup different simulation domains are considered.

Fig. 1 shows the final simulation domain of a NMC_{111}-graphite full cell with perforated electrodes. In our simulations we make use of the symmetry of the perforation pattern in order to save computational resources. At the boundary of the computational domain we apply no-flux conditions for heat, mass, and charge in y- and z-directions. Similar simulation domains were also chosen by Chen[8] and Habedank *et al.*[24] in their simulations with homogenized models. The dimensions of the simulation domain considered in the present paper are 210 x 100 x 100 µm using cubic voxels with a voxel size of around 0.876 µm. The galvanostatic charge and discharge simulations are performed at different C-rates in order to evaluate the effect of perforation on cell performance. Note that for perforated cells we use the same current density as in the reference case to provide a consistent comparison of the concepts. Moreover, we focus on ideally aligned hole configurations but provide an estimate on the effect of misalignment in Section 3.4.

In the symmetric cell setup two identical anode and cathode microstructures are facing each other. This setup has been extensively used in the literature to determine the tortuosity of electrodes.[40,47,50] In our simulations we evaluate the influence of the perforation on effective

electrode transport parameters. A description of the simulation procedure for impedance simulations is provided in Ref.[48]

3 Results and discussion

In this section we present the results of our electrochemical simulations using different cell setups. First, we use impedance simulations on symmetric cells to determine the pore transport resistance of each electrode in the unperforated reference state as well as the perforated state. Then, full cell impedance simulations are analyzed to determine the effect of perforation on the overall cell resistance. In a next step we present results of isothermal as as well as thermal galvanostatic cycling simulations in full cell configuration. During charge, particular attention will be paid to the analysis of electrolyte and active material concentration distributions and to the risk of lithium plating. Finally, we investigate the influence of deviations from our idealized cell setup using electrodes with perfectly aligned cylindrical holes. These studies provide insights on different aspects related to the realization of the perforation concept in a production process.

3.1 Impedance simulations

3.1.1 Symmetric cell

In our electrochemical impedance simulations of symmetric cells (EIS-SC) we determine the ionic pore transport resistance of the virtual electrodes prepared in this work. For homogeneous samples the pore transport resistance which is given by the effective electrolyte conductivity can also be determined by simpler transport simulations.[48] However, for the inhomogeneous perforated electrode structures investigated in this work this approach is not applicable. Therefore, the impedance simulations provide a better description of the relevant transport processes occurring in the battery during operation.

Fig. 2 a) shows the impedance spectra of symmetric NMC_{111} cells for both the reference

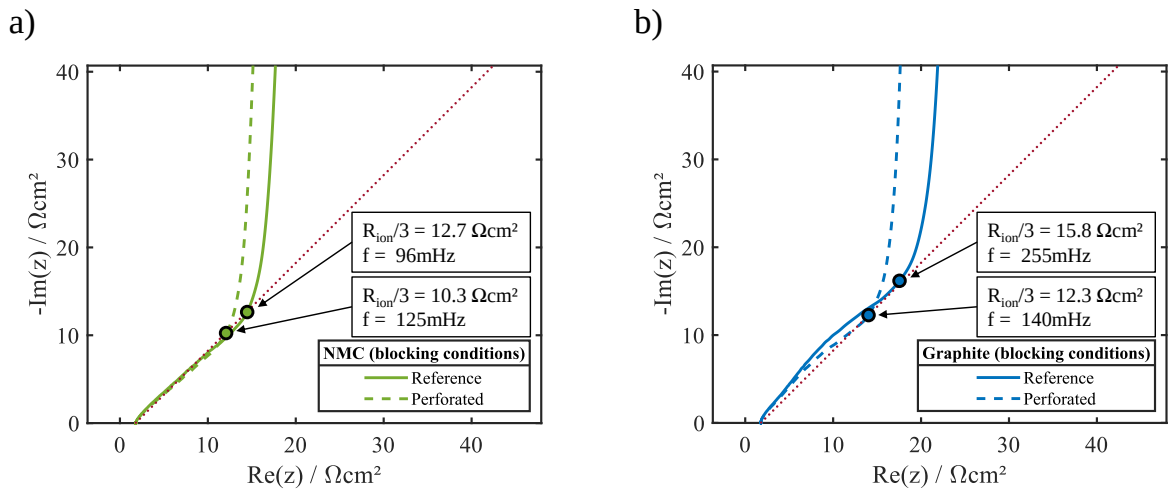

Figure 2: a) Impedance spectra of symmetric NMC_{111} cells (99% SoC) made of perforated (dashed line) and unperforated electrodes (solid line) under blocking conditions. b) Impedance spectra of reference (solid line) and perforated (dashed line) graphite electrodes enforcing blocking conditions. The contribution of the electrolyte accounts for R_{elyte}=1.8 $\Omega\,cm^2$ in both cases. A dashed red line with an angle of 45° to the real axis is included as guide for the eye.

(solid line) and perforated electrodes (dashed line). In order to suppress contributions of Faradaic processes in our simulations we set the initial lithium concentrations in the active material close to the fully lithiated state (SoC of 0.99). Under these conditions the slope of the OCV is large (ca. -135.03 V/SoC) and small perturbations in potential result in negligible Faradaic currents. These conditions are often referred to as blocking conditions, i.e. allowing no charge transfer across the solid/electrolyte interface. In experiments this situation is often ensured by using non-intercalating salts.[40] The Nyquist plot of a symmetric cell under ideally blocking conditions is supposed to show a straight 45° increase of the imaginary part at high frequencies followed by a vertical line at low frequencies due to the blocking conditions.[51] The intersection of the linear increase with the vertical line can be used to determine the pore transport resistance of the electrodes.[51]

The impedance spectra of the symmetric NMC_{111} cells presented in Fig. 2 a) show close to ideal behavior. At high frequencies the simulations perfectly match the 45° increase indicated by the red dotted line. In our simulations the perforation decreases the overall pore

transport resistance which can be seen by a shift of the intersection between the first part (45° line) and the second part (vertical line) to the left. This demonstrates that the hierarchical pore space introduced by the perforation indeed improves transport of lithium ions in the electrolyte by around 19%.

In our simulations we use a consistent set of parameters for the simulation of both the NMC_{111} and graphite electrodes to ensure the same blocking conditions during the impedance simulations in the symmetric setup. Impedance spectra of symmetric graphite cells are shown in Fig. 2 b). The graphite electrodes show a slight deviation from the expected behavior of ideally blocking electrodes (dashed red line) at high frequencies. We assign this deviation from ideal behavior to a microstructural effect probably caused by the particle shape and size distribution of graphite. Similar impedance spectra are also reported in [15]. Overall, the pore transport resistance of the graphite electrodes is slightly larger compared to the NMC_{111} electrodes. In this case perforation is able to reduce the pore transport resistance by around 22%.

3.1.2 Full-cell

In the previous section we demonstrated that laser perforation of the electrodes is able to reduce the pore transport resistance. However, on the other hand, by removing active material we also reduce the specific active surface area which increases the charge transfer resistance. Both effects contribute adversely to the overall impedance of the full cell setup.

Fig. 3 a) shows impedance spectra of NMC_{111}-graphite full cells for varying SoC. The reference configuration and perforated electrodes are represented by solid and dashed lines, respectively. Despite the loss in active surface area, it is evident that perforation is able to reduce the overall impedance of the cell. Thus, the increase in charge transfer resistance is smaller compared to the reduced pore transport resistance. This is also illustrated in Fig. 3 b). The green curve represents an ideal case where the cell resistance of the unperforated NMC_{111}-graphite reference cell at a frequency of 1 mHz is corrected by the reduction in trans-

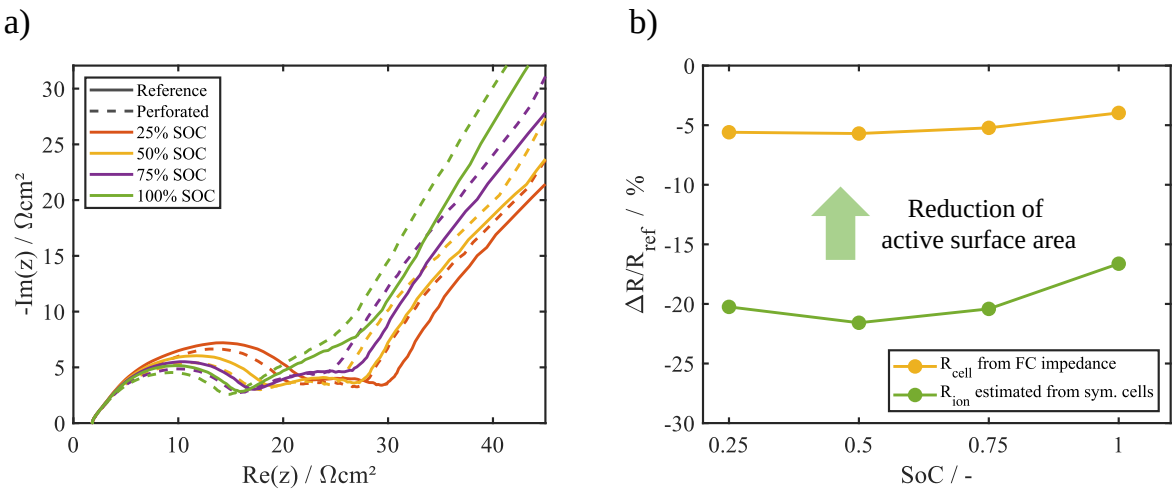

Figure 3: a) Impedance spectra of NMC_{111}-graphite full cell, for different SoCs in the frequency range from 100 kHz-1 mHz. b) Relative resistance of the perforated cell compared to the unperforated reference. Green line: Estimated improvements in cell resistance based on the pore transport resistance R_{ion} of the symmetric cells. Yellow line: Relative cell resistance derived from the simulation of the NMC_{111}-graphite full cells.

port resistance R_{ion} determined by the simulations of symmetric graphite and NMC_{111} cells. These two contributions add up to an overall reduction in resistance of around 8.85 Ωcm^2. Combining the data provides the optimum you can expect neglecting the negative effects of the perforation. The yellow curve instead represents the simulated relative decrease in cell resistance of the perforated NMC_{111}-graphite cell. Our simulations demonstrate that in the full cell the decrease in resistance is smaller compared to the ideal case. The difference between the green and yellow curve can be assigned to the decrease in reaction kinetics due to the loss in active surface area.

We emphasize that perforation reduces the overall cell impedance. Therefore, we expect improved cell performance at high currents during galvanostatic operation which is investigated in the following paragraph.

3.2 Galvanostatic operation

In this section we present the simulation results of galvanostatic charge and discharge processes at different currents. The simulations are used to validate performance improvements

of the perforated electrodes indicated by our impedance simulations. First, we focus on idealized isothermal conditions before we also investigate the effect of perforation on heat sources within the cell. The latter is an important aspect for the development of battery packs.

3.2.1 Isothermal conditions

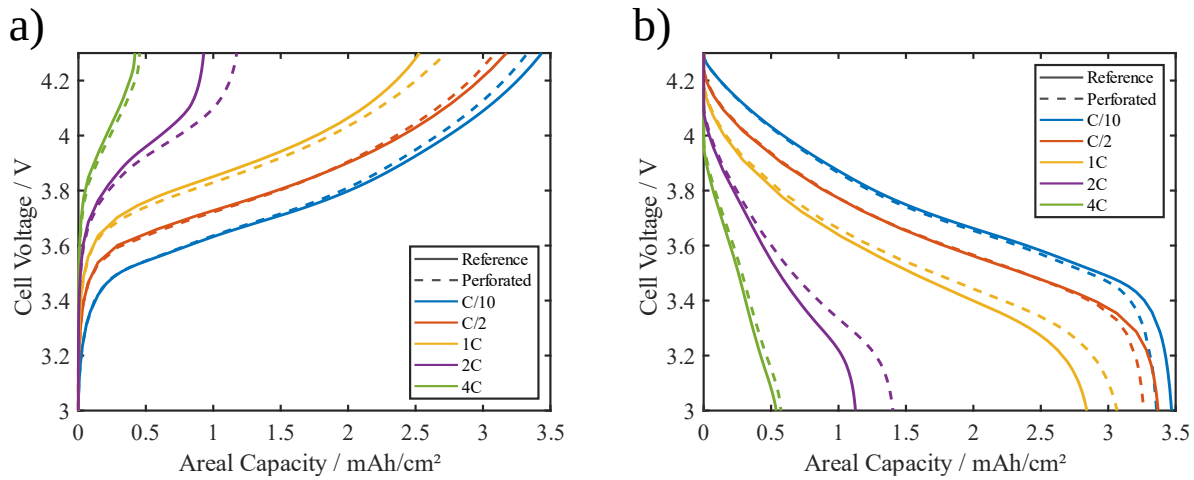

Figure 4: a) Charge and b) discharge curves of NMC_{111}-graphite cells for varying C-rates using conventional (solid line) and perforated (dashed line) electrodes at room temperature (298 K).

Fig. 4 shows a) charge and b) discharge curves of NMC_{111}-graphite full cells at room temperature. At low charging and discharging rates our simulations confirm that perforation reduces the practical capacity of the cell compared to the unperforated reference configuration due to the removal of active material. The loss in active material associated with the perforation process in this work is 3.1% which is only marginally higher compared to the loss in capacity at C/10 rate which is around 3% for both charge and discharge simulations. At higher currents the perforated configuration outperforms the reference configuration which is in line with the corresponding reports in the literature.[8,24,52] In our case the beneficial effects due to improved electrolyte transport in the macroscopic transport channels become important at currents as low as 1C. It is interesting to notice that improvements due to the perforation for the charge and discharge process are not symmetric. In fact the relative

gain in capacity during a 1C discharge is larger compared to the 1C charging process. This effect is mainly due to the choice of cut-off potentials. But also the asymmetric concentration distributions arising from different effective transport and geometric properties of the electrodes contribute to the behavior. Additional spatial distributions of the concentrations are presented in the supporting information in Figs. S9-S10. A more detailed analysis of transport processes in electrodes with high areal loading can also be found in Ref.[47]

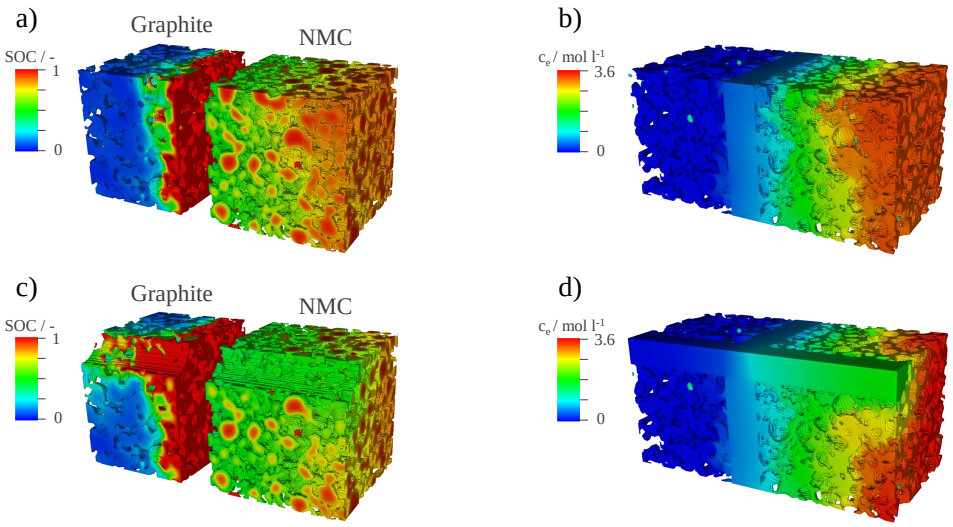

Figure 5: Distribution of local lithium concentrations in the active materials (a,c) and electrolyte (b,d) in reference (top row) and perforated geometries (bottom row) at the end of a 2C constant current charging phase (4.3 V cut-off voltage) at 298 K.

In our discussion we focus on the concentration distributions at high charging currents. Fig. 5 shows the concentrations in the active material (left column) and electrolyte (right column) at end of the 2C charging process. The top row (Figs. 5 a, b) and bottom row (Fig. 5 c, d) represent the reference and perforated setup, respectively. Looking at the concentration distribution in the electrolyte in Figs. 5 b) and d), it is evident how perforation affects electrolyte transport in the cell. In the graphite electrode, we generally see a depletion of the salt in the electrolyte for both the reference and perforated case. Only in the center of the channel slightly higher salt concentrations are predicted for the perforated electrode. In the cathode the effect of the perforation is more pronounced. In the vicinity of the hole the salt

concentration is lower compared to the reference case. This highlights the beneficial effect due to the macroscopic channels created by laser perforation.

The salt distribution in the electrolyte directly influences the lithium concentration distribution in the active material. Figs. 5 a) and b) show the normalized lithium concentration in graphite and NMC particles. In the unperforated NMC electrode the local SoC distribution is rather homogeneous with slightly higher concentrations close to the current collector. However, at the negative electrode only the graphite close to the separator interface is lithiated. This confirms that the performance of the cell is limited by the transport of lithium ions in the graphite electrode. Perforation of the electrode improves transport in the electrolyte and additional active material close to the hole surface becomes accessible for intercalation. This is illustrated by the red regions in the graphite electrode in Fig. 5 c). This improvement in active material utilization corresponds to an increase in charging capacity of around 25% during constant current (CC) charging.

Similar qualitative effects of the perforation on fast-charging performance are also observed

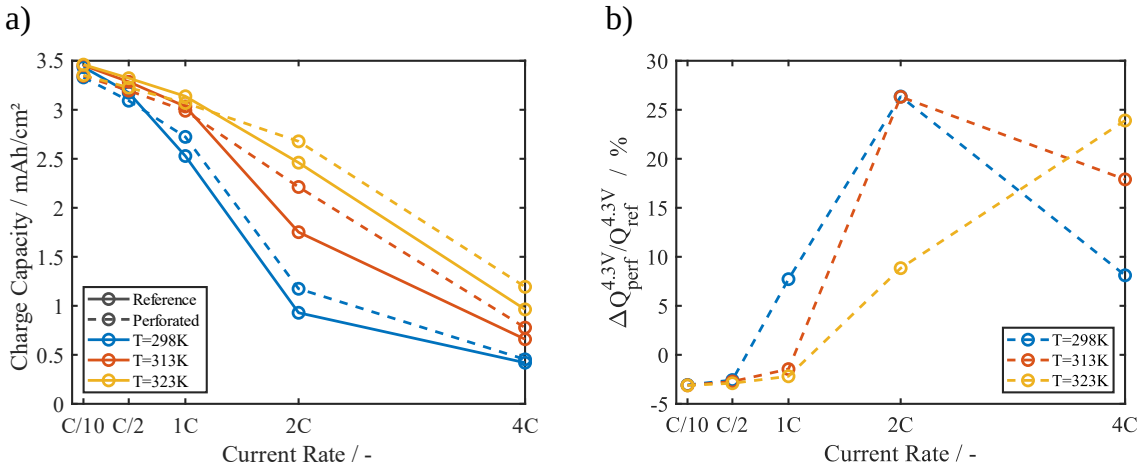

Figure 6: a) Simulated capacity of a constant current charging process for different temperatures and charging rates. Solid and dashed lines indicate results of the reference and perforated setup, respectively. b) Corresponding relative gain in capacity of the perforated cell setup.

at higher temperatures. The simulated areal capacities at the end of the constant current charge process are summarized in Fig. 6 a). The blue lines representing the simulations at

room temperature show a significant drop in capacity at charging currents corresponding to a 2C rate. At higher temperatures this drop in capacity is less pronounced. This effect is related to improved ion mobility at higher temperatures which mitigates transport limitations in the electrolyte. This has an immediate effect on the relative gain in charge capacity which is shown in Fig. 6 b). At higher temperatures (see Fig. S6) the beneficial effect of the perforation becomes visible only at charging currents above 1C. Here we observe a maximum gain in our simulations at 298 K and 313 K reaching up to 25% capacity improvement. At higher currents mainly the surface of the graphite electrode is active due to almost complete salt depletion in the electrolyte. Therefore, the beneficial effect of improved transport in the holes is less pronounced. Interestingly, this maximum is shifted at 323 K even beyond the currents investigated in this work. Still, we do not expect major improvements at higher currents, neither relative nor absolute, since the CC charging capacity shown in Fig. 6 a) decreases nearly linearly at high currents and temperatures.

The simulations presented in this paragraph indicate that already a moderate increase in cell temperature is able to improve fast-charging performance. Therefore, we investigate in the next section the evolution of temperature and the influence of perforation on the most significant heat sources in the cell.

3.2.2 Thermal simulations

In this section we investigate the effect of the perforation on the heat generated during fast charging and the resulting cell temperature. As indicated in the previous paragraph increasing cell temperatures do also have a noticeable influence on the resulting CC capacity predicted by our simulations. Fig. 7 shows thermal simulations using different charging rates with an initial cell temperature of 298 K. All other initial conditions are the same like in the isothermal simulations. As indicated in Fig. 7 a) charging characteristics are similar to the isothermal case. Still, we see an improvement of fast-charging performance of the perforated electrodes. Especially for a 2C charging rate, the areal capacity is a factor of two larger

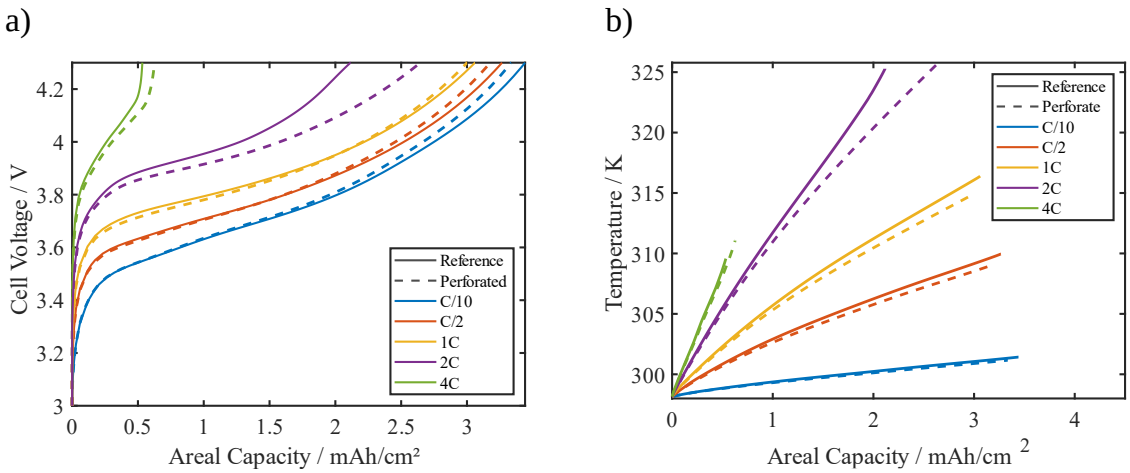

Figure 7: a) Charging curves of NMC_{111}-graphite full- cells with an initial temperature of 298 K and b) corresponding evolution of the average cell temperature.

compared to perforated electrodes under isothermal conditions.

A direct comparison between isothermal and thermal charging curves can also be found in Fig. S5. Fig. 7 b) shows the corresponding evolution of the average cell temperature during charge. In our simulations we do not see major temperature gradients on the cell level. Spatial distributions of temperatures and heat sources can also be found in Fig. S11 in the SI. Since we apply adiabatic boundary conditions in our simulations we see at all currents an increase in cell temperature which becomes more prominent at higher rates. Also, we observe that the cell temperature is slightly lower in the case of perforated electrodes. However, differences are minor and can be mainly attributed to reduced heat generation in the electrolyte.

Therefore, we conclude that a moderate increase in cell temperature due to internal heat sources improves fast-charging performance. However, perforation does not provide an additional benefit compared to the improvements already seen for isothermal simulations. For a detailed analysis of the thermal behavior of whole cells and battery packs this analysis is not comprehensive enough. Still, our simulations indicate that structural modification on electrode level will not have a significant impact on the overall thermal behavior. Another interesting aspect closely linked to the cell temperature is the probability of lithium plating

in the cell. In the next section we will analyze the risk of lithium plating at high charging currents and provide a qualitative analysis on the influence of electrode perforation on the probability, and location of plated lithium in the cell.

3.3 Plating

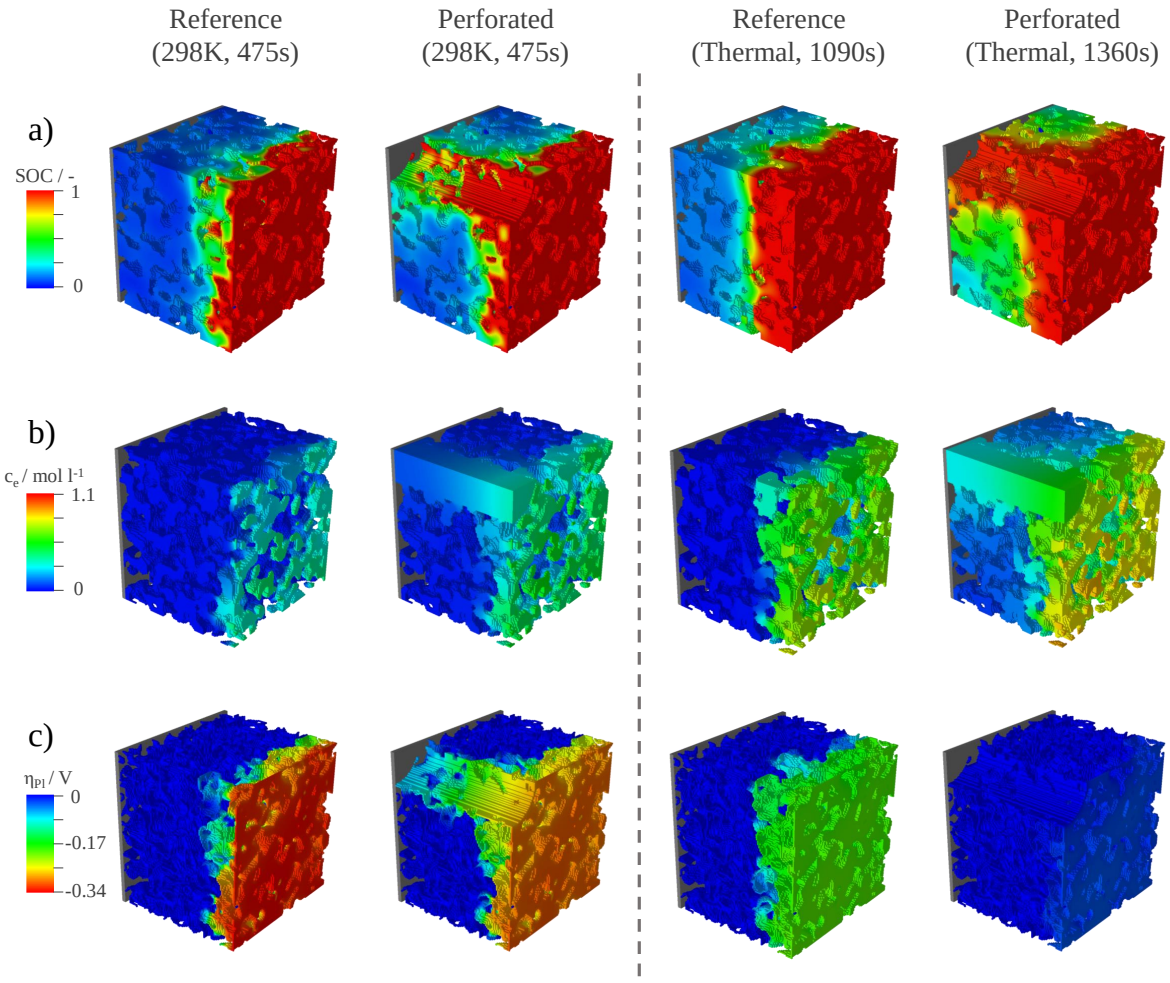

Figure 8: Distributions of a) graphite SoC, b) electrolyte concentration and c) plating overpotential during a 2C charging process. At the top of each column the respective simulation set up is indicated. The left two columns show isothermal simulations after 475 s when the unperforated cell exceeds the upper cut-off voltage of 4.3 V ($Q_{ref,iso} = 0.9$ mAh cm^{-2}). The right two columns show thermal simulations, where the 4.3 V cut-off is reached after 1090 s and 1360 s for the reference and perforated electrodes, respectively ($Q_{ref,th} = 2.1$ mAh cm^{-2} and $Q_{perf,th} = 2.6$ mAh cm^{-2}).

Lithium plating is one of the major degradation mechanisms in lithium ion batteries

during fast charging. Due to the relatively low lithium mobility in the active material, especially at low temperatures, the composition at the particle surfaces rapidly reaches one lithium atom per C_6. The OCV of this highly lithiated graphite phase is close to 0 V vs lithium metal. Due to additional kinetic losses the local potential step at the electrode electrolyte interface becomes negative. In our formulation this potential step corresponds to the overpotential of the lithium metal plating and stripping reaction [53]

$$\eta_{\mathrm{Pl}} = \Phi_{\mathrm{So}} - \varphi_{\mathrm{El}}^{\mathrm{Li}^+} + \mathrm{U}_0^{\mathrm{nuc}} < 0. \tag{11}$$

Note that a negative potential step at the interface is a necessary condition but not sufficient to predict lithium plating. Additional nucleation barriers ($\mathrm{U}_0^{\mathrm{nuc}}$) or kinetic limitations might prevent the formation of a metallic lithium phase. In the literature additional plating overpotentials of up to $\mathrm{U}_0^{\mathrm{nuc}} = 30\,\mathrm{mV}$ are reported depending on the substrate. [54,55] The corresponding plating current is then given by

$$\mathrm{i}_{\mathrm{Plating}} = \mathrm{i}_{\mathrm{Plating}}^{00} \cdot \sqrt{\mathrm{c}_{\mathrm{El}}} \left(\exp\left(\frac{\mathrm{F}}{2\mathrm{RT}} \cdot \eta_{\mathrm{Plating}} \right) - \exp\left(-\frac{\mathrm{F}}{2\mathrm{RT}} \cdot \eta_{\mathrm{Plating}} \right) \right) \tag{12}$$

Once the plating barriers are overcome, however, the exponential dependence of the plating current on the overpotential causes fast lithium plating. In our study we neglect additional barriers ($\mathrm{U}_0^{\mathrm{nuc}} = 0$). In addition to a negative overpotential also a non-vanishing concentration of lithium ions is needed close to the surface for the deposition of a metallic lithium phase. Therefore, the three decisive parameters for the analysis of lithium plating during fast charging are the lithium concentration in the active material or local SoC, the lithium ion concentration in the electrolyte, and the overpotential of the plating reaction.

Fig. 8 gives an overview of these three decisive parameters towards the end of a 2C charging process. The risk for plating is highest at lower temperatures. Therefore, we focus on isothermal simulations at room temperature comparing the unperforated and perforated

setup. As discussed in the previous paragraph high charging currents will also increase the cell temperature. Therefore, we additionally analyze thermal simulations which are shown in the last two columns of Fig. 8. Note that the first two columns represent snapshots at 475 s, corresponding to the end of the CC charge process of the reference setup at 298 K.

The first row in Fig. 8 shows the local SoC in the active material. In the isothermal simulations of the perforated, as well as the unperforated electrode, we see complete lithiation close to the separator surface. In the perforated electrode the hole walls are also almost completely lithiated. In the thermal simulations the increase in temperature improves transport processes in both the electrolyte and active material. Still, at the end of the constant current charging process (1090 s) the surface of the graphite electrode close to the separator is completely lithiated and regions close to the current collector are not utilized. In contrast, the thermal simulations of the perforated electrodes show a much higher utilization of the region close to the current collector, which is in line with the increase in capacity reported in the previous paragraph.

The corresponding distributions of lithium ions in the electrolyte are shown in the second row of Fig. 8. In the unperforated electrodes we observe very low salt concentrations close to the current collector. Only next to the separator there is still some non-vanishing lithium concentration. In the perforated electrode, salt concentrations are overall slightly higher. Major improvements can be observed in the thermal simulations due to the increase in temperature. In this case, even close to the current collector, the concentration of lithium ions is larger than 0.1 mol/l. Low lithium ion concentrations might initially prevent or reduce a deposition of metallic lithium. In a latter stage it was shown that such conditions can promote dendrite growth following the gradient in concentration.[56]

Finally, overpotential distributions are shown in the last row of Fig. 8. Here, the difference between the unperforated reference and the perforated electrode is significant. In the reference case plating overpotentials close to the separator interface exceed 300 mV which is sufficient to overcome thermodynamic and kinetic nucleation barriers.[55] In contrast, the

overpotentials in the perforated electrodes are much lower. Nevertheless, in the isothermal simulations at 298 K we see negative overpotentials which indicate a risk for lithium plating. The thermal simulations show that even the slight increase in temperature observed in our simulations is able to reduce the risk of lithium plating (see Fig. 8). Critical conditions can be avoided in the first phase of the charging process and much smaller negative overpotentials are observed during charge to the upper cut-off limit ($\eta_{\mathrm{lPl}} = 170\,\mathrm{mV}$). Perforation of the electrodes has a significant effect on the plating overpotential in the thermal simulations. Even at the upper cut-off limit plating potentials are negligible and below reported values of nucleation barriers. Most likely perforation will help to avoid lithium plating under these conditions.

Overall, our simulations demonstrate that perforation is a very effective strategy to reduce lithium plating during fast-charging of the battery. This result is in excellent agreement with the observations of Chen *et al.* and Kriegler *et al.*[8,16] who reported significant improvements in cycle life.

3.4 Influence of hole shape and configuration

In previous paragraphs we demonstrated that cells consisting of structured electrodes with perfectly aligned cylindrical holes show improved performance and a lower tendency for lithium plating during fast charging. However, during cell manufacturing, especially on an industrial scale, both the ideal cylindrical hole shape as well as an ideal alignment are challenging to realize and and thus deviations from the optimal case are expected. Moreover, in most experimental studies only the graphite anode is perforated to improve fast-charging performance.[8,16] Recent simulation work suggests that structuring of both electrodes,[28] provides additional improvements in fast-charging performance. Therefore, we investigate in this paragraph the influence of hole shape and alignment and additionally benchmark the performance of symmetrically perforated electrodes to cells with a perforated graphite anode only.

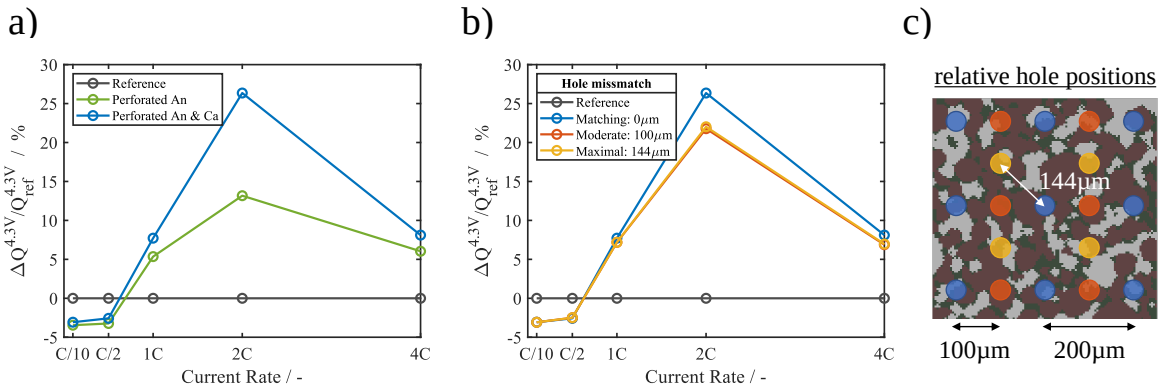

Figure 9: a) Gain in relative charge capacity for cells with unperforated electrodes (black), symmetrically perforated electrodes (blue) and perforated anode only (green). b) Gain in relative charge capacity for different configurations representing misalignment of laser holes. c) Corresponding schematic image illustrating the relative positions of ideally aligned (blue) holes and configurations with moderate (red) and maximal (yellow) misalignment. All simulations are performed under isothermal conditions at 298 K.

3.4.1 Influence of symmetrical perforation

Fig. 9 a) shows the relative gain in constant current charge capacity for three different electrode configurations. The unperforated reference cell is shown in black color. The green line represents the cell with a perforated anode only. The simulations show that perforation of the anode already improves the capacity during the constant current charging phase by up to 13%. However, perforation of both electrodes always provides superior performance. Maximum improvements of around around 27% are observed at a 2C charging rate. This is twice as high compared to the cell with perforation only on the anode side and demonstrates that improved transport in the cathode additionally enhances cell performance during charging. Note that in the case with only a perforated anode we adjust the thickness of the unperforated cathode in order to provide the same nominal capacity compared to a symmetrically perforated cell.

3.4.2 Influence of misalignment

The misalignment of the laser induced holes is an issue which can be hardly avoided during stacking of the electrodes. Therefore, we investigate the influence of two representative cases

of misalignment on cell performance.

Fig. 9 b) shows the relative gain in charging capacity curves for two different configurations representing two extreme cases of misalignment. Both cases are illustrated in Fig. 9 c). In the first case (red color) the holes are shifted by 100 µm resulting in a relative position between two holes on the opposite electrode side. In the second case the hole sits directly in the center between the four opposite holes (yellow color), which is the maximum distance of hole centers compared to the ideally aligned case (blue color). The simulations show that the effect of misalignment on charging performance is moderate. Still, it can reduce the beneficial effect of the perforation by around 5% at a 2C charging rate. The differences between the misaligned configurations are minor.

In addition to the negative effect on capacity, misalignment also results in a local imbalance between anode and cathode which might cause lithium plating during fast charging. In our simulations we also analyze the risk of lithium plating for the different configurations considered above. However, local fluctuations in the plating overpotential (Eq. 11) on the surface to the separator are minor and stay within 7% of the average plating overpotential. This result indicates that misalignment on this rather small scale does not have a major impact on degradation phenomena. The corresponding distributions of η_{Pl} at the end of the charging process are shown in the supporting information.

3.4.3 Influence of hole geometry

Another issue arising during the manufacturing process is the realization of ideal cylindrical hole shapes. In the following, we consider the influence of tapered holes with different entrance angles. In all cases the tapered holes have the same volume resulting in approximately the same electrode capacity (see inlets i-iv) in Fig. 10. First we investigate the effect of the entrance angle on the pore transport resistance. For this purpose, we simulate impedance spectra of symmetrically perforated graphite cells following the setup described in Section 3.1.1. Fig. 10 a) shows a Nyquist plot of simulated impedance spectra. The black line

represents the unperforated graphite reference and the different colors from blue to orange represent increasing entrance angles. For small angles ($< 20°$) the hole depth is still close to the electrode thickness and we do not observe a relevant increase in pore transport resistance. However, with increasing angle the resistance rises and at 60° the reduction in pore transport resistance between the structured electrode and the unperforated reference electrode is only 50% compared to the reduction with ideal cylindrical holes. This trend is also reflected in the fast-charging performance. Fig. 10 b) shows the difference in charge capacity relative to an electrode with ideal cylindrical holes. Similar to the impedance deviations are minor for small angles. In fact we observe a slight increase in charge capacity for an angle of 20°. However, for angles larger than 20° differences become noticeable with a maximum reduction in capacity of up to 6%. For a 2C charging current the improvement in capacity of the cylindrical pores compared to the unperforated reference is 13%. Therefore, despite the reduction of capacity due to deviations from an ideal cylindrical hole shape, perforation still promises improvements in fast-charging performance.

These studies indicate that the conical shape does not have a significant impact on fast-charging performance as long as the depth of the holes is still close to the thickness of the electrodes. From a fabrication point of view this might allow for faster processing without compromising the benefits of the structuring approach.

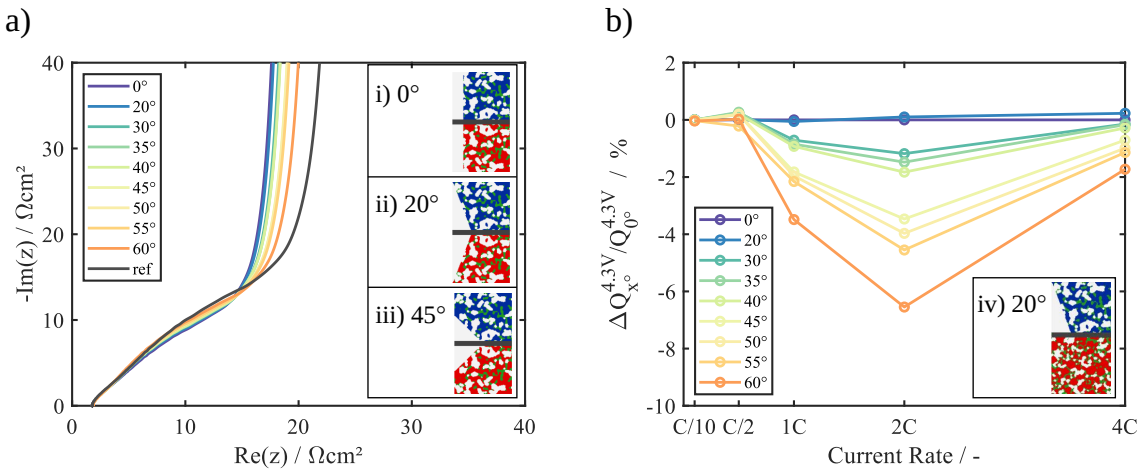

Figure 10: a) Simulated symmetrical impedance spectra of cone shaped holes with increasing entrance angle. b) Corresponding difference in relative charge capacity with respect to a cylindrical hole (0°). All perforated electrodes have the same capacity and simulations are performed under isothermal conditions at 298 K. i)-iv) Schematic cross sections with graphite (blue), NMC_{111} (red) and CBD (green).

4 Summary and Conclusions

A sufficiently good fast-charging performance is a key property of the battery to promote the breakthrough of battery electric vehicles. However, at the same time improvements in fast-charging performance should not come at the cost of a reduction of energy density. Several structuring concepts are suggested in the literature in order to resolve this dilemma. In this paper we investigate the effect of electrode perforation on the capacity, temperature evolution, and degradation in lithium ion batteries using microstructure resolved simulations.

Our simulations demonstrate that perforation is able to improve the fast-charging performance which is measured as capacity which can be charged into the cell during the CC charging phase. This is an important criteria since it is indicative for the overall duration of the charge process. This improvement can be mainly attributed to a reduction in pore transport resistance which is quantified by simulating impedance spectra in a symmetric cell setup. Although improvements in the CC capacity reach up to 25% the major advantage of the perforation is a significant reduction of the risk for lithium plating. Our simulations suggest that suitable perforation concepts are able to significantly improve the cycle life of

Li-ion batteries which are charged at high rates. This is in good agreement with results reported in the literature.

In our studies we set a focus on perfectly aligned cylindrical holes in order to evaluate improvements under ideal conditions. In an industrial production process deviations from this ideal case can be expected. We simulate different scenarios including conical holes and misalignment to estimate the effect on fast-charging performance. Generally, deviations from the ideal setup cause a decrease in fast-charging performance. Still, in all cases the performance as well as the tendency towards lithium plating are improved compared to unperforated electrodes.

In the future we will apply our modeling and simulation tool to investigate optimal hole configurations and protocols for fast-charging of lithium-ion batteries. We will combine our studies with our recently developed detailed degradation models.[53] Additionally, improvements for models on the material level need to be developed to include e.g. staging or anisotropic diffusion and interacalation in graphite. These extensions will give us the opportunity to quantitatively study and mitigate the main aging mechanisms during fast-charging.

Acknowledgement

The authors acknowledge support by the state of Baden-Württemberg through bwHPC and the German Research Foundation (DFG) through grant no INST 40/467-1 FUGG (JUSTUS cluster). The presented work was financially supported by the BMBF within the project HiStructures under the grant number 03XP0243D/E. This work contributes to the research performed at CELEST (Center for Electrochemical Energy Storage Ulm-Karlsruhe).

Supporting Information Available

The following files are available free of charge.

- FastchargingLIBs-SI.pdf: List of electrochemical parameters, Simulated charge curves, concentration and potential distributions, distribution of heat sources and temperatures

References

(1) Plötz, P.; Gnann, T.; Wietschel, M. Modelling market diffusion of electric vehicles with real world driving data—Part I: Model structure and validation. *Ecological Economics* **2014**, *107*, 411–421.

(2) Plötz, P.; Axsen, J.; Funke, S. A.; Gnann, T. Designing car bans for sustainable transportation. *Nature Sustainability* **2019**, *2*, 534–536.

(3) Longo, M.; Zaninelli, D.; Viola, F.; Romano, P.; Miceli, R. How is the spread of the Electric Vehicles? 1st International Forum on Research and Technologies for Society and Industry Leveraging a better tomorrow (RTSI). 2015; pp 439–445.

(4) Ahmed, S.; Bloom, I.; Jansen, A. N.; Tanim, T.; Dufek, E. J.; Pesaran, A.; Burnham, A.; Carlson, R. B.; Dias, F.; Hardy, K.; Keyser, M.; Kreuzer, C.; Markel, A.; Meintz, A.; Michelbacher, C.; Mohanpurkar, M.; Nelson, P. A.; Robertson, D. C.; Scoffield, D.; Shirk, M.; Stephens, T.; Vijayagopal, R.; Zhang, J. Enabling fast charging – A battery technology gap assessment. *Journal of Power Sources* **2017**, *367*, 250–262.

(5) Gallagher, K. G.; Trask, S. E.; Bauer, C.; Woehrle, T.; Lux, S. F.; Tschech, M.; Lamp, P.; Polzin, B. J.; Ha, S.; Long, B.; Wu, Q.; Lu, W.; Dees, D. W.; Jansen, A. N. Optimizing Areal Capacities through Understanding the Limitations of Lithium-Ion Electrodes. **2015**, *163*, A138–A149.

(6) Zeng, X.; Li, M.; Abd El-Hady, D.; Alshitari, W.; Al-Bogami, A. S.; Lu, J.; Amine, K. Commercialization of lithium battery technologies for electric vehicles. *Advanced Energy Materials* **2019**, *9*, 1900161.

(7) Billaud, J.; Bouville, F.; Magrini, T.; Villevieille, C.; Studart, A. R. Magnetically aligned graphite electrodes for high-rate performance Li-ion batteries. *Nature Energy* **2016**, *1*, 1–6.

(8) Chen, K.-H.; Namkoong, M. J.; Goel, V.; Yang, C.; Kazemiabnavi, S.; Mortuza, S.; Kazyak, E.; Mazumder, J.; Thornton, K.; Sakamoto, J.; Dasgupta, N. P. Efficient fast-charging of lithium-ion batteries enabled by laser-patterned three-dimensional graphite anode architectures. *Journal of Power Sources* **2020**, *471*, 228475.

(9) Patry, G.; Romagny, A.; Martinet, S.; Froelich, D. Cost modeling of lithium-ion battery cells for automotive applications. *Energy Science & Engineering* **2015**, *3*, 71–82.

(10) Pfleging, W. A review of laser electrode processing for development and manufacturing of lithium-ion batteries. *Nanophotonics* **2018**, *7*, 549–573.

(11) Du, Z.; Wood, D. L.; Daniel, C.; Kalnaus, S.; Li, J. Understanding limiting factors in thick electrode performance as applied to high energy density Li-ion batteries. *Journal of Applied Electrochemistry* **2017**, *47*, 405–415.

(12) Zhao, R.; Liu, J.; Gu, J. The effects of electrode thickness on the electrochemical and thermal characteristics of lithium ion battery. *Applied Energy* **2015**, *139*, 220–229.

(13) Gao, H.; Wu, Q.; Hu, Y.; Zheng, J. P.; Amine, K.; Chen, Z. Revealing the rate-limiting li-ion diffusion pathway in ultrathick electrodes for li-ion batteries. *The Journal of Physical Chemistry Letters* **2018**, *9*, 5100–5104.

(14) Danner, T.; Singh, M.; Hein, S.; Kaiser, J.; Hahn, H.; Latz, A. Thick electrodes for Li-ion batteries: A model based analysis. *Journal of Power Sources* **2016**, *334*, 191–201.

(15) Park, J.; Jeon, C.; Kim, W.; Bong, S.-J.; Jeong, S.; Kim, H.-J. Challenges, laser processing and electrochemical characteristics on application of ultra-thick electrode for high-energy lithium-ion battery. *Journal of Power Sources* **2021**, *482*, 228948.

(16) Kriegler, J.; Hille, L.; Stock, S.; Kraft, L.; Hagemeister, J.; Habedank, J. B.; Jossen, A.; Zaeh, M. F. Enhanced performance and lifetime of lithium-ion batteries by laser structuring of graphite anodes. *Applied Energy* **2021**, *303*, 117693.

(17) Kraft, L.; Habedank, J. B.; Frank, A.; Rheinfeld, A.; Jossen, A. Modeling and Simulation of Pore Morphology Modifications using Laser-Structured Graphite Anodes in Lithium-Ion Batteries. **2019**, *167*, 013506.

(18) Li, L.; Erb, R. M.; Wang, J.; Wang, J.; Chiang, Y.-M. Fabrication of low-tortuosity ultrahigh-area-capacity battery electrodes through magnetic alignment of emulsion-based slurries. *Advanced Energy Materials* **2019**, *9*, 1802472.

(19) Nemani, V. P.; Harris, S. J.; Smith, K. C. Design of bi-tortuous, anisotropic graphite anodes for fast ion-transport in Li-ion batteries. *Journal of The Electrochemical Society* **2015**, *162*, A1415.

(20) Sakamoto, J. S.; Dunn, B. Hierarchical battery electrodes based on inverted opal structures. *Journal of Materials Chemistry* **2002**, *12*, 2859–2861.

(21) Bae, C.-J.; Erdonmez, C. K.; Halloran, J. W.; Chiang, Y.-M. Design of battery electrodes with dual-scale porosity to minimize tortuosity and maximize performance. *Advanced materials* **2013**, *25*, 1254–1258.

(22) Sander, J.; Erb, R. M.; Li, L.; Gurijala, A.; Chiang, Y.-M. High-performance battery electrodes via magnetic templating. *Nature Energy* **2016**, *1*, 1–7.

(23) US Department of Energy, Battery500: Progress Update. 2020; `https://www.energy.gov/eere/articles/battery500-progress-update`.

(24) Habedank, J. B.; Kraft, L.; Rheinfeld, A.; Krezdorn, C.; Jossen, A.; Zaeh, M. F. Increasing the discharge rate capability of lithium-ion cells with laser-structured graphite

anodes: modeling and simulation. *Journal of The Electrochemical Society* **2018**, *165*, A1563.

(25) Habedank, J. B.; Kriegler, J.; Zaeh, M. F. Enhanced fast charging and reduced lithium-plating by laser-structured anodes for lithium-ion batteries. *Journal of The Electrochemical Society* **2019**, *166*, A3940.

(26) Habedank, J. B.; Schwab, D.; Kiesbauer, B.; Zaeh, M. F. Paving the way for industrial ultrafast laser structuring of lithium-ion battery electrodes by increasing the scanning accuracy. *Journal of Laser Applications* **2020**, *32*, 022053.

(27) Usseglio-Viretta, F.; Mai, W.; Colclasure, A.; Doeff, M.; Yi, E.; Smith, K. Enabling fast charging of lithium-ion batteries through secondary- /dual- pore network: Part I - Analytical diffusion model. *Electrochimica Acta* **2020**, *342*, 136034.

(28) Mai, W.; Usseglio-Viretta, F. L.; Colclasure, A. M.; Smith, K. Enabling fast charging of lithium-ion batteries through secondary-/dual- pore network: Part II - numerical model. *Electrochimica Acta* **2020**, *341*, 136013.

(29) ITWM, BEST - Battery and Electrochemistry Simulation Tool. 2020; `http://itwm.fraunhofer.de/best`.

(30) Latz, A.; Zausch, J. Thermodynamic consistent transport theory of Li-ion batteries. *Journal of Power Sources* **2011**, *196*, 3296–3302.

(31) Latz, A.; Zausch, J. Thermodynamic derivation of a Butler–Volmer model for intercalation in Li-ion batteries. *Electrochimica Acta* **2013**, *110*, 358–362.

(32) Latz, A.; Zausch, J. Multiscale modeling of lithium ion batteries: thermal aspects. *Beilstein Journal of Nanotechnology* **2015**, *6*, 987–1007.

(33) Ji, Y.; Zhang, Y.; Wang, C.-Y. Li-ion cell operation at low temperatures. *Journal of The Electrochemical Society* **2013**, *160*, A636.

(34) Lundgren, H.; Behm, M.; Lindbergh, G. Electrochemical characterization and temperature dependency of mass-transport properties of LiPF6 in EC: DEC. *Journal of The Electrochemical Society* **2014**, *162*, A413.

(35) Tippmann, S.; Walper, D.; Balboa, L.; Spier, B.; Bessler, W. G. Low-temperature charging of lithium-ion cells part I: Electrochemical modeling and experimental investigation of degradation behavior. *Journal of Power Sources* **2014**, *252*, 305–316.

(36) Cui, S.; Wei, Y.; Liu, T.; Deng, W.; Hu, Z.; Su, Y.; Li, H.; Li, M.; Guo, H.; Duan, Y.; Wang, W.; Rao, M.; Zheng, J.; Wang, X.; Pan, F. Optimized Temperature Effect of Li-Ion Diffusion with Layer Distance in Li(NixMnyCoz)O2 Cathode Materials for High Performance Li-Ion Battery. *Advanced Energy Materials* **2016**, *6*, 1501309.

(37) Srinivasan, V.; Wang, C. Analysis of electrochemical and thermal behavior of Li-ion cells. *Journal of The Electrochemical Society* **2002**, *150*, A98.

(38) Loges, A.; Herberger, S.; Seegert, P.; Wetzel, T. A study on specific heat capacities of Li-ion cell components and their influence on thermal management. *Journal of Power Sources* **2016**, *336*, 341–350.

(39) Werner, D.; Loges, A.; Becker, D. J.; Wetzel, T. Thermal conductivity of Li-ion batteries and their electrode configurations–A novel combination of modelling and experimental approach. *Journal of Power Sources* **2017**, *364*, 72–83.

(40) Landesfeind, J.; Hattendorff, J.; Ehrl, A.; Wall, W. A.; Gasteiger, H. A. Tortuosity determination of battery electrodes and separators by impedance spectroscopy. *Journal of The Electrochemical Society* **2016**, *163*, A1373–A1387.

(41) Pang, H.; Zhang, F. Experimental data-driven parameter identification and state of charge estimation for a Li-ion battery equivalent circuit model. *Energies* **2018**, *11*, 1033.

(42) Yu, Q.-Q.; Xiong, R.; Wang, L.-Y.; Lin, C. A comparative study on open circuit voltage models for lithium-ion batteries. *Chinese Journal of Mechanical Engineering* **2018**, *31*, 65.

(43) Westhoff, D.; Manke, I.; Schmidt, V. Generation of virtual lithium-ion battery electrode microstructures based on spatial stochastic modeling. *Computational Materials Science* **2018**, *151*, 53–64.

(44) Feinauer, J.; Brereton, T.; Spettl, A.; Weber, M.; Manke, I.; Schmidt, V. Stochastic 3D modeling of the microstructure of lithium-ion battery anodes via Gaussian random fields on the sphere. *Computational Materials Science* **2015**, *109*, 137–146.

(45) Adler, R. *The Geometry of Random Fields*; Classics in Applied Mathematics; Society for Industrial and Applied Mathematics (SIAM), Philadelphia, 1981.

(46) Chiu, S.; Stoyan, D.; Kendall, W.; Mecke, J. *Stochastic Geometry and Its Applications*; Wiley Series in Probability and Statistics; J. Wiley & Sons, Chichester, 2013.

(47) Kremer, L. S.; Danner, T.; Hein, S.; Hoffmann, A.; Prifling, B.; Schmidt, V.; Latz, A.; Wohlfahrt-Mehrens, M. Influence of the electrolyte salt concentration on the rate capability of ultra-thick NCM 622 electrodes. *Batteries & Supercaps* **2020**, *3*, 1172–1182.

(48) Hein, S.; Danner, T.; Westhoff, D.; Prifling, B.; Scurtu, R.; Kremer, L.; Hoffmann, A.; Hilger, A.; Osenberg, M.; Manke, I.; Wohlfahrt-Mehrens, M.; Schmidt, V.; Latz, A. Influence of Conductive Additives and Binder on the Impedance of Lithium-Ion Battery Electrodes: Effect of Morphology. **2020**, *167*, 013546.

(49) Kremer, L. S.; Hoffmann, A.; Danner, T.; Hein, S.; Prifling, B.; Westhoff, D.; Dreer, C.; Latz, A.; Schmidt, V.; Wohlfahrt-Mehrens, M. Manufacturing process for improved ultra-thick cathodes in high-energy lithium-ion batteries. *Energy Technology* **2020**, *8*, 1900167.

(50) Hein, S.; Latz, A. Influence of local lithium metal deposition in 3D microstructures on local and global behavior of lithium-ion batteries. *Electrochimica Acta* **2016**, *201*, 354–365.

(51) Itagaki, M.; Suzuki, S.; Shitanda, I.; Watanabe, K. Electrochemical impedance and complex capacitance to interpret electrochemical capacitor. *Electrochemistry* **2007**, *75*, 649–655.

(52) Park, J.; Hyeon, S.; Jeong, S.; Kim, H.-J. Performance enhancement of Li-ion battery by laser structuring of thick electrode with low porosity. *Journal of Industrial and Engineering Chemistry* **2019**, *70*, 178–185.

(53) Hein, S.; Danner, T.; Latz, A. An electrochemical model of lithium plating and stripping in lithium ion batteries. *ACS Applied Energy Materials* **2020**, *3*, 8519–8531.

(54) Pei, A.; Zheng, G.; Shi, F.; Li, Y.; Cui, Y. Nanoscale nucleation and growth of electrodeposited lithium metal. *Nano Letters* **2017**, *17*, 1132–1139.

(55) Gao, T.; Han, Y.; Fraggedakis, D.; Das, S.; Zhou, T.; Yeh, C.-N.; Xu, S.; Chueh, W. C.; Li, J.; Bazant, M. Z. Interplay of lithium intercalation and plating on a single graphite particle. *Joule* **2021**, *5*, 393–414.

(56) Tan, J.; Cannon, A.; Ryan, E. Simulating dendrite growth in lithium batteries under cycling conditions. *Journal of Power Sources* **2020**, *463*, 228187.

Graphical TOC Entry